UNIVERSITAT POLITÈCNICA DE CATALUNYA
BARCELONATECH

UPCommons

Portal del coneixement obert de la UPC

http://upcommons.upc.edu/e-prints

Aquesta és una còpia de la versió *author's final draft* d'un article publicat a la revista *International Journal of Heat and Mass Transfer.*

URL d'aquest document a UPCommons E-prints:

http://hdl.handle.net/2117/119649

Article publicat / *Published paper*:

Bartrons, E., [et al.]. A finite volume method to solve the frost growth using dynamic meshes. *International journal of heat and mass transfer*, 1 Setembre 2018, vol. 124, p. 615-628. DOI: <10.1016/j.ijheatmasstransfer.2018.03.104>.

© <2018>. Aquesta versió està disponible sota la llicència CC-BY-NC-ND 4.0 http://creativecommons.org/licenses/by-nc-nd/4.0/

A finite volume method to solve the frost growth using dynamic meshes

Eduard Bartrons[a,b,*], Carles Oliet[a], Enrique Gutiérrez[a,b], Alireza Naseri[a], Carlos David Pérez-Segarra[a,**]

[a] *Heat and Mass Transfer Technological Center, Universitat Politècnica de Catalunya, Carrer de Colom 11, 08222 Terrassa (Barcelona), Spain*
[b] *Termo Fluids, S.L., Av. Jaquard 97 1-E, 08222 Terrassa (Barcelona), Spain*

Abstract

The physical mechanisms of frost formation have been widely studied, yet much empirism is still needed in numerical approaches. Indeed, accurate simulations of frost growth can be reached by setting up a specific combination of the model empirical inputs while using a method to accurately track the frost-air interface.

This paper presents a finite volume ALE method which captures the air-frost interface using dynamic meshes. It is divided into two main sections. First, the search of a valid set of empirical correlations to correctly emulate frost growth under certain experimental conditions. An assessment of seven reference cases is carried out by comparing solutions using different empirical correlations against experimental data. As a result, a discussion on the performance of such parameters is made, emphasizing the fact of using diffusion resistance factors above 1.0 in order to capture the frost growth. Second, a 2D numerical test consisting of a duct flow with a non-homogeneously cooled lower boundary is performed. Aspects related to the frost thickness and growth rate are analysed, proving the method to be a valid candidate to simulate frost growth.

Keywords: Frost growth, Arbitrary Lagrangian-Eulerian (ALE) method, Dynamic mesh, Numerical model, Diffusion resistance factor

Nomenclature

c_p	specific heat capacity, J/(kgK)
D	diffusivity, m^2/s
D_h	hydraulic diameter, m
h	enthalpy, J/kg
h_{sv}	latent heat of sublimation, J/kg

*Eduard Bartrons
**Carlos David Pérez-Segarra
Email addresses: eduard@cttc.upc.edu (Eduard Bartrons), cttc@cttc.upc.edu (Carlos David Pérez-Segarra)

h_c	convective heat transfer coefficient, W/(m^{2}K)
h_m	mass transfer coefficient, m/s
$\vec{j}$	diffusion mass flux, kg/(m^{2}s)
$\dot{m}$	water vapour mass flux, kg/(m^{2}s)
$\dot{q}$	heat flux, W/m^2
$\mathbf{r}$	vector of residuals
S	supersaturation degree
T	temperature, K (Celsius when specified)
P	pressure, Pa
v	velocity, m/s
V	volume, m^3
W	water vapour concentration, $\mathrm{kg_v/kg_{da}}$
x	mole fraction
$\mathbf{x}$	vector of variables
y	coordinate, m
Y_v	water vapour concentration, $\mathrm{kg_v/kg_{ha}}$

Greek symbols

α_r	relaxation factor
δ	relative error
δy	mesh displacement, m
Δy_{fs}	growth displacement, m
ε	porosity
λ	conductivity, W/mK
μ	diffusion resistance factor
ρ	density, kg/m^3
τ	tortuosity
$\dot{\omega}_i$	ice generation, kg/(m^{3}s)
$\dot{\omega}_v$	water vapour generation, kg/(m^{3}s)

Subscript

av	averaged
da	dry air
dens	related to the densification of the frost layer
Δy	related to the increase of layer thickness
eff	effective
fl	frost layer (contains ice and humid air)
fs	frost surface
ha	humid air
i	ice
lat	latent
sat	saturated
t	total
v	water vapour
w	wall
x	related to the position in streamwise direction
0	initial value

∞ far field conditions

Superscript

ℓ current outer iteration

m current inner iteration

n current time step

q iteration

1. Introduction

Whenever a surface is in contact with humid air below the dew and freezing points, water vapour will desublimate, transitioning to a solid state that will form a crystaline structure called frost. Frost formation is a common and usually undesired phenomenon that affects the aerospace, cryogenics and refrigeration industry, among others. Frost can form on aircraft wings either on-ground (typically through nocturnal frost), and in-flight (when crossing supersaturated icing clouds [1]), adding weight and reducing the aerodynamical performance. It also causes a great impact on wind turbines, heat exchangers, engine turbine blades, electrical lines, etc. These issues highlight the need of understanding and accurately predicting frost formation.

Hayashi *et al.* [2] divided the frost formation mechanism into three periods: the *crystal growth period*, the *frost layer growth period* and the *frost layer full growth period*. The first refers to an early growth period characterized by crystal growth. First, heterogeneous nucleation and further embryo growth covers the cold wall as a thin frost layer. In the second period, the frost layer behaves as a porous medium, where crystals continue growing while interacting with each other. In this period, the initial rough frost becomes a uniform layer. It is considered to end when the thickness of the frost stops growing. The third period continues with a densification and growth of the frost layer, bringing with it an increase of the thermal resistance [2]. During that stage, the thickness growth is minimal, and the frost surface temperature rises until the melting point. From that point onwards, new deposition sites at the frost surface will form in liquid phase, which will soak into the frost layer, freezing in the inside. This cycle process continues periodically until the heat transfer condition reaches the equilibrium.

The frost layer growth period is the most studied among the three. Brian *et al.* [3] proposed first analytical approximations to model frost growth. Later on, Tao *et al.* [4] and Le Gall *et al.* [5] used averaged finite volume approaches, which were also used by Na and Webb [6] with some simplifications. Na and Webb's formulation was subsequently used by Lenic *et al.* [7], and recently by Armengol *et al.* [8] to address the air-frost coupled problem. Other significant approaches involving the computation of the fluid and frost domains are the coupling of a one dimensional frost model with a comercial CFD code by Ellgas and Pfitzner [9], the one-domain approach by Kim *et al.* [10], in which

the one dimensional frosting model [11] is implemented, and the recent frost formation resistance model put forward by Kim *et al.* [12].

Despite the efforts to simulate the frost-free air coupled problem, there is still a lack of consensus in which empirical correlations capture better the frost formation. Furthermore, solutions with CFD approaches use static grids [7, 8, 13, 14, 15, 16], which lead to a non-accurate tracking of the interface.

In view of the reported results, a finite volume approach based on Tao's mathematical formulation, which models the frost layer growth period (until the melting point is reached) using a deformable mesh is here presented. This paper aims to discuss the performance of the tested empirical correlations, and provide new insights throughout a critical analysis of seven reference cases, covering a wide range of experimental conditions. Finally, the stated methodology is used to numerically solve the frosting on a wind tunnel with a non-homogeneously cooled lower boundary, experimentally set up by Kwon *et al.* [17], in order to test the model capabilities.

2. Physical model and mathematical formulation

The mechanism of frost growth is shown in Fig. 1, in which a local averaged control volume analysis is depicted. The set out approach considers that a volume V is composed by the volumes occupied by the ice V_i, and the humid air V_{ha}. The ice volume fraction or ice porosity is then defined as $\varepsilon_i = V_i/V$. Similarly, the air porosity is expressed as $\varepsilon_{\mathrm{ha}} = V_{\mathrm{ha}}/V$. Moreover, the equalty $\varepsilon_{\mathrm{ha}} + \varepsilon_i = 1$ must be preserved. In addition, note that the humid air porosity, the dry air porosity and the water vapour porosity stand for the same volume fraction, i.e., $\varepsilon_{\mathrm{ha}} = \varepsilon_{\mathrm{da}} = \varepsilon_v$. Such porosities will also be represented as ε_v for the sake of clarity.

The assumptions made in the present analysis are: (a) the total gas phase pressure P_{ha} is constant throughout the porous frost layer, and equal to the external atmospheric pressure P_∞; (b) water vapour, dry air and ice are in local thermal equilibrium, i.e. $T_{\mathrm{ha}} = T_v = T_{\mathrm{da}} = T_i$; (c) water vapour inside the frost layer is saturated; (d) the heat and mass transfer analogy is applicable, with a constant Lewis number; (e) convection effects are negligible such that $\vec{v}_{\mathrm{ha}} = 0$ within the frost layer [18], and (f) no movement of the ice crystals is allowed ($\vec{v}_i = 0$).

2.1. The transport diffusion equations

The vapour mass conservation equation reads as:

$$\frac{\mathrm{d}}{\mathrm{d}t}\int_{V_v} \rho_v \mathrm{d}V_v + \int_{S_v} \rho_v \left(\vec{v}_v - \vec{v}_b\right)\cdot \vec{n}\mathrm{d}S_v = \int_{V} \dot{\omega}_v \mathrm{d}V \tag{1}$$

where the substantial derivative of the Eulerian density field including the volume swept by the mesh equals the generation or destruction of water vapour $\dot{\omega}_v$. Integrating over the volume V and rewriting the equation in terms of the water vapour diffusion mass flux $\vec{j}_v = \rho_v\left(\vec{v}_v - \vec{v}_{ha}\right)$.

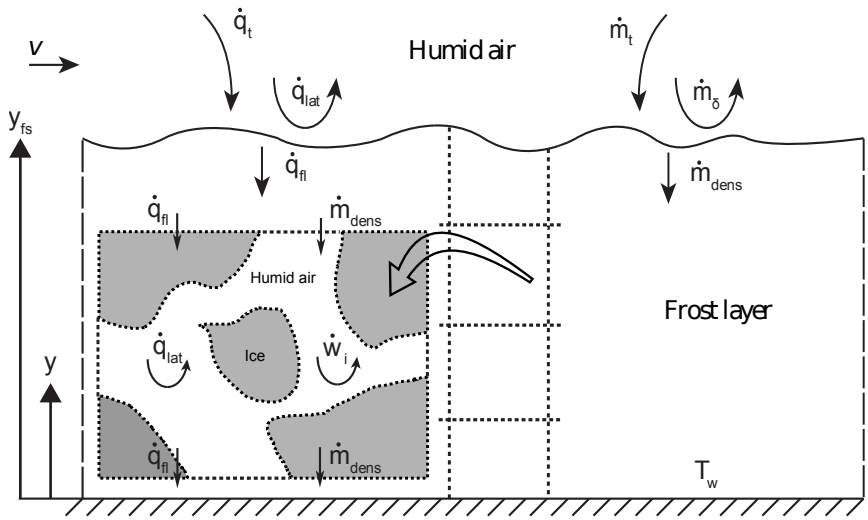

Figure 1: Sketch of the frost growth in a discretized domain. The detail of the elementary control volume shows the implemented averaged volume technique.

$$\frac{\mathrm{d}}{\mathrm{d}t}\int_V \rho_v \varepsilon_v \mathrm{d}V + \int_S \rho_v \varepsilon_v \left(\vec{v}_{\mathrm{ha}} - \vec{v}_b\right)\cdot \vec{n}\mathrm{d}S + \int_S \varepsilon_v \vec{j}_v \vec{n}\mathrm{d}S = \int_V \dot{\omega}_v \mathrm{d}V \tag{2}$$

Applying that $\vec{v}_{ha} = 0$ and introducing Fick's law, i.e. $\vec{j}_v = -\rho_{ha}\tau D_v \nabla Y_v$:

$$\frac{\mathrm{d}}{\mathrm{d}t}\int_V \rho_v \varepsilon_v \mathrm{d}V - \int_S \rho_v \varepsilon_v \vec{v}_b \cdot \vec{n}\mathrm{d}S = \int_S \rho_{\mathrm{ha}} \varepsilon_v \tau D_v \nabla Y_v \cdot \vec{n}\mathrm{d}S + \int_V \dot{\omega}_v \mathrm{d}V \tag{3}$$

where Y_v is the concentration of water vapour, and τ is the tortuosity. The effective diffusivity is defined as $D_{\mathrm{eff}} \equiv \varepsilon_v \tau D_v$ or $D_{\mathrm{eff}} \equiv \mu D_v$, where μ is called the diffusion resistance factor ($\mu \equiv \varepsilon_v \tau$). On the other hand, setting up the transport equation of the ice phase:

$$\frac{\mathrm{d}}{\mathrm{d}t}\int_V \rho_i \varepsilon_i \mathrm{d}V + \int_S \rho_i \varepsilon_i \left(\vec{v}_i - \vec{v}_b\right)\cdot \vec{n}\mathrm{d}S = \int_V \dot{\omega}_i \mathrm{d}V \tag{4}$$

where ice generation equals water vapour destruction ($\dot{\omega}_i = -\dot{\omega}_v$). Applying the equality into Eq.4 and substituting into Eq. 3, while considering $\vec{v}_i = 0$, and rearranging the terms:

$$\frac{\mathrm{d}}{\mathrm{d}t}\int_V \varepsilon_v\left(\rho_v-\rho_i\right)\mathrm{d}V-\int_S \varepsilon_v\left(\rho_v-\rho_i\right)\vec{v}_b\cdot\vec{n}\mathrm{d}S=\int_S \rho_i\vec{v}_b\vec{n}\mathrm{d}S \\ -\frac{\mathrm{d}}{\mathrm{d}t}\int_V \rho_i\mathrm{d}V+\int_S \rho_{\mathrm{ha}}D_{\mathrm{eff}}\nabla Y_v\cdot\vec{n}\mathrm{d}S \tag{5}$$

2.2. The energy equation

The energy conservation equation is given by the following equation:

$$\frac{\mathrm{d}}{\mathrm{d}t}\sum_k\int_{V_k}\left(\rho_k h_k-P_k\right)\mathrm{d}V_k+\sum_k\int_{S_k}\rho_k h_k\left(\vec{v}_k-\vec{v}_b\right)\cdot\vec{n}\mathrm{d}S_k=-\sum_k\int_{S_k}\vec{\dot{q}}_k\cdot\vec{n}\mathrm{d}S_k \tag{6}$$

where $k=\{i,v,\mathrm{da}\}$. Rewriting the former in terms of the diffusion mass flux $\vec{j}_r=\rho_r\left(\vec{v}_r-\vec{v}_{\mathrm{ha}}\right)$, where $r=\{v,\mathrm{da}\}$, and applying the condition $P_{\mathrm{ha}}\approx P_i\approx P_\infty$ as well as the assumed zero velocities of the ice and humid air within the frost layer:

$$\frac{\mathrm{d}}{\mathrm{d}t}\int_V\left(\varepsilon_i\rho_i h_i+\varepsilon_v\rho_{\mathrm{ha}}h_{\mathrm{ha}}\right)\mathrm{d}V-\int_S\left(\varepsilon_i\rho_i h_i+\varepsilon_v\rho_{\mathrm{ha}}h_{\mathrm{ha}}\right)\vec{v}_b\cdot\vec{n}\mathrm{d}S \\ +\int_S\varepsilon_v h_v\vec{j}_v\cdot\vec{n}\mathrm{d}S+\int_S\varepsilon_v h_{\mathrm{da}}\vec{j}_{\mathrm{da}}\cdot\vec{n}\mathrm{d}S=-\int_S\left(\varepsilon_i\vec{\dot{q}}_i+\varepsilon_{\mathrm{ha}}\vec{\dot{q}}_{\mathrm{ha}}\right)\cdot\vec{n}\mathrm{d}S \tag{7}$$

Now, developing the enthalpy cross-diffusion terms:

$$\frac{\mathrm{d}}{\mathrm{d}t}\int_V\left(\varepsilon_i\rho_i h_i+\varepsilon_v\rho_{\mathrm{ha}}h_{\mathrm{ha}}\right)\mathrm{d}V-\int_S\left(\varepsilon_i\rho_i h_i+\varepsilon_v\rho_{\mathrm{ha}}h_{\mathrm{ha}}\right)\vec{v}_b\cdot\vec{n}\mathrm{d}S \\ +\int_S\varepsilon_v\left(h_v-h_{\mathrm{da}}\right)\vec{j}_v\cdot\vec{n}\mathrm{d}S=-\int_S\left(\varepsilon_i\vec{\dot{q}}_i+\varepsilon_{\mathrm{ha}}\vec{\dot{q}}_{\mathrm{ha}}\right)\cdot\vec{n}\mathrm{d}S \tag{8}$$

where $\vec{j}_v=-\vec{j}_{\mathrm{da}}$. Furthermore, defining the frost layer (fl) conduction heat flux as $\vec{\dot{q}}_{\mathrm{fl}}\equiv\varepsilon_i\vec{\dot{q}}_i+\varepsilon_{\mathrm{ha}}\vec{\dot{q}}_{\mathrm{ha}}$ and applying Fick's law:

$$\frac{\mathrm{d}}{\mathrm{d}t}\int_V\left(\varepsilon_i\rho_i h_i+\varepsilon_v\rho_{\mathrm{ha}}h_{\mathrm{ha}}\right)\mathrm{d}V-\int_S\left(\varepsilon_i\rho_i h_i+\varepsilon_v\rho_{\mathrm{ha}}h_{\mathrm{ha}}\right)\vec{v}_b\cdot\vec{n}\mathrm{d}S= \\ \int_S\left(h_v-h_{\mathrm{da}}\right)\rho_{\mathrm{ha}}D_{eff}\nabla Y_v\cdot\vec{n}\mathrm{d}S-\int_S\vec{\dot{q}}_{\mathrm{fl}}\cdot\vec{n}\mathrm{d}S \tag{9}$$

The enthalpy cross-diffusion term on the right-hand side of the equation is neglected as it is about five orders of magnitude smaller than the heat flux term

$(h_v - h_{\mathrm{da}})\,\rho_{ha} D_{\mathrm{eff}} \nabla Y_v$			$\vec{q}_{\mathrm{fl}} = -\lambda_{\mathrm{fl}} \nabla T$	
$(h_v - h_{\mathrm{da}})$	$\rho_{\mathrm{ha}} D_{\mathrm{eff}}$	∇Y_v	λ_{fl}	∇T
10^7	10^{-7}	10^{-1}	10^1	10^3
10^{-1}			10^4	

Table 1: Orders of magnitude of the right-hand side of Eq. 9.

(see Table 1). Note that this term is not usually mentioned in the literature. Recalling that enthalpies are defined as:

$$h_n = h_{f_n} + \int_{T_{\mathrm{ref}}}^{T} c_{p_n} \mathrm{d}T \approx h_{f_n} + \bar{c}_{p_n} \left(T - T_{\mathrm{ref}}\right) \tag{10}$$

$$\bar{c}_{p_n} = \frac{1}{T - T_{\mathrm{ref}}} \int_{T_{\mathrm{ref}}}^{T} c_{p_n} \mathrm{d}T \tag{11}$$

where $n = \{i, v, \mathrm{da}\}$ and h_f is the formation enthalpy. Rearranging the terms of Eq. 9 in terms of the temperature, the following expression is reached:

$$\begin{aligned} \frac{\mathrm{d}}{\mathrm{d}t} \int_V \left(\mathcal{C}_1 T + \mathcal{C}_2 \varepsilon_v + \mathcal{C}_3 \varepsilon_v T\right) \mathrm{d}V - \int_S \left(\mathcal{C}_1 T + \mathcal{C}_2 \varepsilon_v + \mathcal{C}_3 \varepsilon_v T\right) \vec{v}_b \cdot \vec{n} \mathrm{d}S = \\ \int_S \left(\mathcal{C}_4 + P_\infty\right) \vec{v}_b \cdot \vec{n} \mathrm{d}S + \int_S \lambda_{\mathrm{fl}} \nabla T \vec{n} \mathrm{d}S - \frac{\mathrm{d}}{\mathrm{d}t} \int_V \mathcal{C}_4 \mathrm{d}V \end{aligned} \tag{12}$$

where λ_{fl} is the frost layer conductivity, and the coefficients $\mathcal{C}_1, \mathcal{C}_2, \mathcal{C}_3, \mathcal{C}_4$ are given by:

$$\begin{aligned} \mathcal{C}_1 &= \rho_i \bar{c}_{p_i} \\ \mathcal{C}_2 &= \rho_i \left(\bar{c}_{p_i} T_{\mathrm{ref}_i} - h_{f_i}\right) + \rho_{\mathrm{ha}} \bar{c}_{p_{\mathrm{da}}} T_{\mathrm{ref}_{\mathrm{da}}} \left(Y_v - 1\right) + \rho_{\mathrm{ha}} Y_v \left(h_{f_v} - \bar{c}_{p_v} T_{\mathrm{ref}_v}\right) \\ \mathcal{C}_3 &= \rho_{\mathrm{ha}} \bar{c}_{p_{\mathrm{da}}} \left(1 - Y_v\right) - \rho_i \bar{c}_{p_i} + \rho_{\mathrm{ha}} Y_v \bar{c}_{p_v} \\ \mathcal{C}_4 &= \rho_i \left(h_{f_i} - \bar{c}_{p_i} T_{\mathrm{ref}_i}\right) - P_\infty \end{aligned}$$

2.3. Boundary conditions

Air-frost interface:

An energy balance at the interface gives the temperature at the frost surface (fs):

$$\underbrace{\lambda_{\mathrm{fl}} \frac{\partial T_{\mathrm{fl}}}{\partial n}}_{\dot{q}_{\mathrm{fl}}} = \underbrace{h_c \left(T_\infty - T_{\mathrm{fs}}\right)}_{\dot{q}_t} + \underbrace{\rho_{\mathrm{fl}} \Delta h_{\mathrm{sv}} \frac{\mathrm{d}y_{\mathrm{fs}}}{\mathrm{d}t}}_{\dot{q}_{\mathrm{lat}}} \tag{13}$$

where the sensible heat flux $\dot{q}_{\mathrm{fl}}$, which penetrates into the frost layer, is generated by the heat convection from the surrounding air $\dot{q}_t$ caused by the temperature gradient between the air bulk and the frost surface, and by the latent heat of sublimation $\dot{q}_{\mathrm{lat}}$ given by the desublimation of water vapour at the frost surface.

The Nusselt number correlations used in the present study vary depending on the tested experiment. Further detail on such taken values will be adressed in Section 5.1 and Section 6.

On the other hand, a mass balance at the frost interface allows the evaluation of the frost surface displacement:

$$\underbrace{\rho_{\mathrm{fl}} \frac{\mathrm{d}y_{\mathrm{fs}}}{\mathrm{d}t}}_{\dot{m}_{\Delta y}} = \underbrace{h_m \left(\rho_{v_\infty} - \rho_{v_{\mathrm{fs}}}\right)}_{\dot{m}_t} - \underbrace{\rho_{\mathrm{ha}} D_{\mathrm{eff}} \frac{\partial Y_{v,\mathrm{fl}}}{\partial n}}_{\dot{m}_{\mathrm{dens}}} \tag{14}$$

Notice that the total deposited mass $\dot{m}_t$ breaks into the part that contributes to the growth of the frost thickness $\dot{m}_{\Delta y}$, and the one that densifies the frost layer $\dot{m}_{\mathrm{dens}}$. The mass transfer coefficient h_m is calculated by means of the heat and mass transfer analogy that assumes a Lewis number of 1.

$$h_m = h_c / \left(\rho_{\mathrm{ha},\infty} c_{p,\mathrm{ha},\infty} Le^{2/3}\right) \tag{15}$$

The terms of Eqs. 13 and 14 are graphically shown in Fig. 1.

A major concern is the calculation of the water vapour pressure at the frost surface. Although theoretical analyses state the water vapour must be supersaturated for the phase change to occur, no general method for the calculation of such pressure values has yet been reported. Authors prior to Na and Webb [19], such as [5, 11], used a saturation condition. Na and Web suggested an empirical expression to model the supersaturation degree (see Eq. 16) extracted from linearizing the laminar boundary layer equations.

$$\begin{aligned} S_{\mathrm{fs}} &= 0.808 \left(\frac{P_{v,\infty}}{P_{v,\mathrm{sat},\infty}}\right) \left(\frac{P_{v,\mathrm{sat,fs}}}{P_{v,\mathrm{sat},\infty}}\right)^{-0.657} - 1 \\ &\text{for} \quad T_{\mathrm{fs}} + 14 < T_\infty < T_{\mathrm{fs}} + 20 \quad \text{and} \quad 243.15K < T_{\mathrm{fs}} < 273.15K \end{aligned} \tag{16}$$

where S_{fs} is defined as follows:

$$S_{\mathrm{fs}} = \frac{P_{v,\mathrm{fs}} - P_{v,\mathrm{sat,fs}}}{P_{v,\mathrm{sat,fs}}} \tag{17}$$

Kandula [20] again used a saturation condition claiming that the supersaturation degree is strongly dependent on the surface coating governing the contact angle, and that there is no such information in the reported experimental data.

Another condition was recently used by El Cheikh and Jacobi [21], which uses the total air heat flux acquired at the frost surface. Unfortunately, this condition needs such value from the experiment. Hence, it was not considered, and saturated and supersaturated conditions were tested. Whenever using the supersaturated condition given in Eq.16 and out of range, the saturated condition is applied.

In regards to the frost density, the Neumann type condition used by Na and Webb [6] is applied. Such condition assumes that the gradient of the frost density at the frost surface is zero, i.e. $\partial \rho_{\mathrm{fl}} / \partial n|_{\mathrm{fs}} = 0$.

The cold wall:

The cases tested in this paper consider a Dirichlet type boundary condition, either through an isothermal wall $T = T_w$ in the 1D tests shown in Section 5, or a varying temperature over the wall in the 2D case presented in Section 6. The wall is assumed totally impermeable, such that the water vapour concentration gradient is zero, hence, $\partial Y_v / \partial n|_{\mathrm{w}} = 0$. Moreover, there is no change in porosity, which leads to $\partial \varepsilon_v / \partial n|_{\mathrm{w}} = 0$.

Other boundaries:

Neumann type boundary conditions are chosen for the temperature, water vapour concentration and porosity.

3. Thermo-physical properties

This section is dedicated to the definition of the implemented thermo-physical properties of ice and the humid air mixture, as well as the averaged frost properties used within the porous medium.

3.1. Ice properties

According to Fukusako's thermophysical correlations of ice [22], in the range of -25°C to 0°C, density changes are about 0.3%, while variations in that range for the conductivity and the specific heat are about 12% and 8%, respectively. The correlations of ice thermal conductivity and heat capacity proposed in the aforementioned paper are:

$$\lambda_i = 1.16 \left(1.91 - 8.66 \cdot 10^{-3}\theta + 2.97 \cdot 10^{-5}\theta^2\right) \quad \text{for} \quad 100K \leq T \leq 273K \tag{18}$$

$$c_{p,i} = 1000 \cdot \left(0.185 + 0.689 \cdot 10^{-2}T\right) \quad \text{for} \quad 90K \leq T \leq 273K \tag{19}$$

where θ is in [°C], and T is in $[K]$.

Several tests were carried out by changing the density, conductivity and specific heat capacity from variable to fixed values. Results show negligible variations under density and heat capacity changes. Hence, mean ice density is considered to be $\bar{\rho}_i = 918.9 kg/m^3$. Nevertheless, changes of approximately 2% on the thermal conductivity lead to accumulated mean density errors of approximately 2-3% after 3 hours of simulation time, stressing out the importance of using a variable ice conductivity.

3.2. Humid air properties

Pressure and density:

Due to the lack of information of the water vapour pressure in the inside of the frost layer, many authors assume the saturation condition. El Cheikh and Jacobi [21] used another formulation in which a mass transfer conductance is considered, avoiding the use of the aforementioned condition. Saturated water vapour below the freezing point can be approximated by the correlation given in [23]. Thus, the dry air pressure can be obtained from $P_{\mathrm{da}} = P_{\infty} - P_{v,\mathrm{sat}}$.

The humid air density, which is the sum of water vapour and dry air densities, is then easily calculated by means of the perfect gas law applied to both substances.

Thermal conductivity:

The thermal conductivity of humid air is a mixture of the dry air and water vapour conductivities. It can be calculated by means of the Studnikov expression found in [24].

$$\lambda_{\mathrm{ha}} = \left(x_{\mathrm{da}}\lambda_{\mathrm{da}} + x_v\lambda_v\right)\frac{1 + \left(x_v - x_v^2\right)}{2.75} \tag{20}$$

where x_{da} and x_v are the dry air and water vapour mole fractions.

Dry air and water vapour conductivites are calculated by means of the suggested correlations by [25].

Diffusivity:

The water vapour diffusivity is determined from [26].

$$D_v = 2.11 \cdot 10^{-5}\left(\frac{T}{T_0}\right)^{1.94}\left(\frac{P_0}{P}\right) \quad \text{for} \quad 233.15K \leq T \leq 313.15K \tag{21}$$

where T_0 and P_0 are the reference temperature ($273.15K$) and the reference pressure ($101325Pa$), respectively.

Specific heat capacity:

The specific heat capacity of humid air can be approximated as the sum of the heat capacities of its elements alone:

$$c_{p,\mathrm{ha}} = Y_{\mathrm{da}}c_{p,\mathrm{da}} + Y_v c_{p,v} \tag{22}$$

The dry air and water vapour heat capacities are given by polinomial fits extracted from the experimental data supplied in [27, 28]:

$$c_{p,\mathrm{da}} = a_0 + a_1T + a_2T^2 + a_3T^3 + a_4T^4 \qquad \text{for} \quad 200K \leq T \leq 400K$$

$$c_{p,v} = \frac{1000}{18.01528}\left(b_1 + b_2T + b_3T^2 + b_4T^3\right) \qquad \text{for} \quad 200K \leq T \leq 800K$$

where coefficients are:

$$
\begin{aligned}
a_0 &= +8.858044433595\mathrm{E}+02 & b_1 &= +33.8\mathrm{E}+00 \\
a_1 &= +1.837101847329\mathrm{E}+00 & b_2 &= -0.00795\mathrm{E}+00 \\
a_2 &= -1.011132405598\mathrm{E}-02 & b_3 &= +2.8228\mathrm{E}-05 \\
a_3 &= +2.353255208331\mathrm{E}-05 & b_4 &= -1.3115\mathrm{E}-08 \\
a_4 &= -1.933268229165\mathrm{E}-08 &
\end{aligned}
$$

3.3. Frost properties

The frost domain is comprised of a porous ice crystaline structure that contains humid air. Depending on the environmental conditions, a large diversity of crystals can be formed. Temperature mainly determines whether snow crystals will grow into plates or columns, while higher supersaturations produce more complex structures (an extensive study can be found in Libbrecht's work [29]). This will affect the thermal conductivity of the frost as well as the mass diffusivity of the water vapour throughout the porous structure. In the present averaged volume approach, the former will be treated as an effective conductivity and diffusivity.

Frost density:

The frost density is directly calculated with the local porosity, humid air and ice densities.

$$\rho_{\mathrm{fl}} = \varepsilon_{\mathrm{ha}}\rho_{\mathrm{ha}} + (1-\varepsilon_v)\,\rho_i \tag{23}$$

Frost effective conductivity:

Among the large amount of correlations suggested in the literature (a detailed list can be found in [30, 31]), the three thermal conductivity correlations proposed by Lee *et al.* [32], Na and Webb [6] and Negrelli *et al.* [30] are hereby tested. These are chosen due to being both some of the most widely (see [31]), and also most recently used.

Lee *et al.* [32] gave the following correlation:

$$\lambda_{\mathrm{fl}} = 0.133 + 3.13e^{-4}\rho_{\mathrm{fl}} + 1.6e^{-7}\rho_{\mathrm{fl}}^2 \quad \text{for} \quad \bar{\rho}_{\mathrm{fl}} \leq 500kg/m^3 \tag{24}$$

Later studies by Na and Webb [6] in the line of the series-parallel model put forward by Sanders [33] suggest that:

$$\lambda_{\mathrm{fl}} = \xi\lambda_{\mathrm{par}} + (1-\xi)\,\lambda_{\mathrm{ser}} \tag{25}$$

where:

$$
\begin{aligned}
\lambda_{\mathrm{par}} &= \left(1-\frac{\rho_{\mathrm{fl}}}{\rho_i}\right)\lambda_{\mathrm{ha}} + \frac{\rho_{\mathrm{fl}}}{\rho_i}\lambda_i \\
\lambda_{\mathrm{ser}} &= \left[\frac{\rho_{\mathrm{fl}}}{\rho_i}\frac{1}{\lambda_i} + \left(1-\frac{\rho_{\mathrm{fl}}}{\rho_i}\right)\frac{1}{\lambda_{\mathrm{ha}}}\right]^{-1}
\end{aligned}
$$

	Range	ξ
(i)	$-10 < T_w < -4$ °C	$0.283 + e^{-0.020\rho_{\mathrm{fl}}}$
(ii)	$-21 < T_w < -10$ °C	$0.140 + 0.919e^{-0.0142\rho_{\mathrm{fl}}}$
(iii)	$T_w < -21$ °C and $\rho_{\mathrm{fl}} < 200\mathrm{kg/m^3}$	$0.0107 + 0.419e^{-0.00424\rho_{\mathrm{fl}}}$
(iv)	$T_w < -21$ °C and $\rho_{\mathrm{fl}} > 200\mathrm{kg/m^3}$	$0.005\rho_{\mathrm{fl}}\left(0.0107 + 0.419e^{-0.00424\rho_{\mathrm{fl}}}\right)$

Table 2: ξ parameter of Na and Webb's effective thermal conductivity correlation.

	Temperature range	Morphology	a	b
(i)	$-10 < T_w < -4$ °C	Needles and sheaths	1.576	0.797
(ii)	$-19 < T_w < -10$ °C	Plates and dentrites	1.594	0.761
(iii)	$-30 < T_w < -19$ °C	Sheaths	1.035	0.797

Table 3: Coefficients of Eq. 26.

And the modeled ξ parameter is given in Table 2.

Negrelli *et al.* [30] have recently introduced a new correlation which takes into account the morphology of the crystals by means of the temperature and the porosity of the frost.

$$\frac{\lambda_{\mathrm{fl}}}{\lambda_i} = a\left(\frac{\lambda_{\mathrm{ha}}}{\lambda_i}\right)^{b\varepsilon_v} \quad \text{for} \quad 0.5 \leq \varepsilon_v \leq 0.95 \tag{26}$$

Coefficients a and b are listed in Table 3. For convenience, the three presented correlations will be referred in this paper as Lee, Na and Webb and Negrelli.

A comparison of the three correlations is depicted in Fig. 2. Whenever Negrelli's correlation is used, and due to the fact that this correlation does not cover the 0 to 1 porosity range, constant thermal conductivity values are set below 0.5 and above 0.95 porosity values, with the values obtained at these two porosities. This treatment is also applied to Lee's correlation when having averaged densities above $500kg/m^3$.

Frost effective diffusivity:

As deduced in Section 2.1, the effective diffusivity is a function of the local porosity, water vapour diffusivity and the tortuosity factor, or just a function of the diffusion resistance factor and the water vapour diffusivity. The tortuosity factor and the diffusion resistance factor are measures of the added difficulty to the water vapour following diffusion paths through the snow crystals. Values above unity contradict reality, as it seems that the water vapour would be able to follow a path shorter than a straight line. However, in the past Tao *et al.* [4] and Le Gall *et al.* [5] used correlations with values higher than 1. Yosida [34]

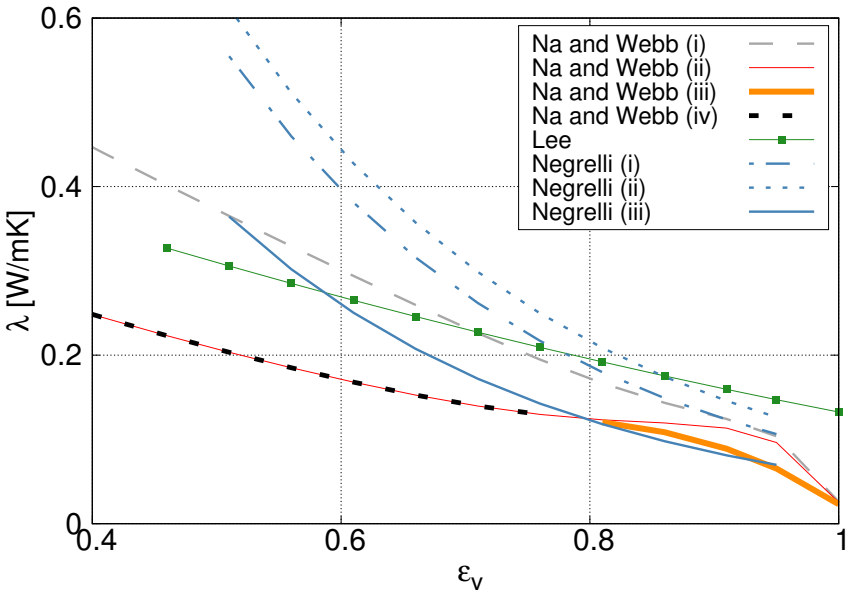

Figure 2: Comparison of frost conductivity correlations as a function of the porosity at $T = 240K$ (influence of temperature is minimal).

also suggested a hand-to-hand delivery of water vapour as an explanation of such diffusion enhancements.

In this paper, the most widely used correlations for the diffusion resistance factor have been tested. All of them are listed in Table 4. Moreover, Fig. 3 shows the calculated values which range from below 1 to 2.2.

Note that the correlations given by Bruggeman, Prager and Zehnder were obtained by means of experimental data of packed beds, not frost. Auracher was the only one to provide a correlation by means of experimental data of frost. However, notice that Auracher did not provide experimental values above $\varepsilon = 0.89$. Either Tao *et al.* [4] and Le Gall *et al.* [5] used modifications of Auracher's correlation to correctly capture the evolution of the frost layer under high porosity values. Further discussion is given in Section 5.2.

4. Numerical implementation

The presented formulation has been implemented into the in-house C++ computer code called TermoFluids. TermoFluids is an unstructured finite volume flow solver, designed for direct and large-eddy numerical simulation of turbulent flows along with multiphysics problems. The reader is referred to [37] for details on the TermoFluids framework that are beyond the scope of this paper.

Author	Diffusion resistance factor
Bruggeman *et al.* [35]	$\mu = \varepsilon_v^{2/3}$
Prager *et al.* [35]	$\mu = 0.5\varepsilon_v\,(1+\varepsilon_v)$
Zehnder *et al.* [33]	$\mu = \left(1-\sqrt{1-\varepsilon_v}\right)$
Auracher *et al.* [36]	$\mu = \varepsilon_v/\left(1-0.58\,(1-\varepsilon_v)\right)$
Le Gall *et al.* [5]	$\mu = \varepsilon_v/\left(1-0.58\,(1-\varepsilon_v)\right) + F10\,(1-\varepsilon_v)\,\varepsilon_v^{10}$

Table 4: Correlations of the diffusion resistance factor.

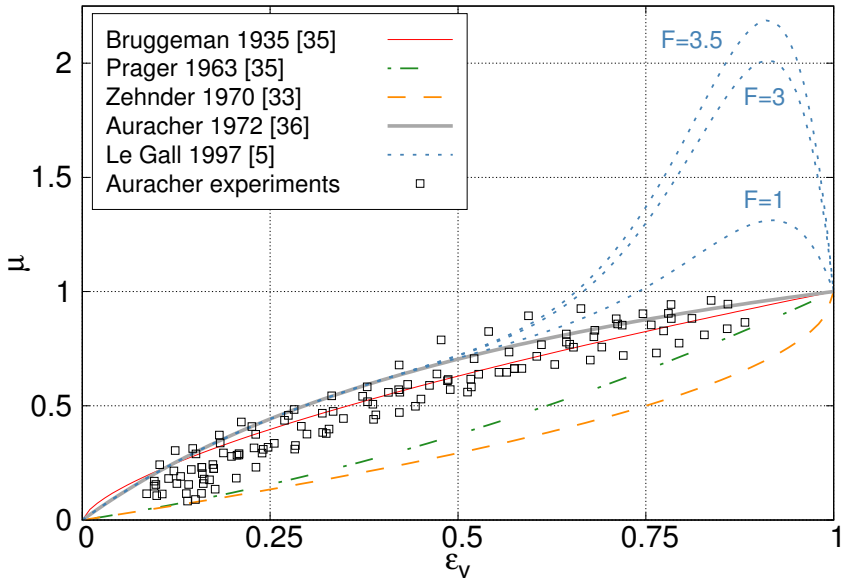

Figure 3: Correlations by various authors of the diffusion resistance factor as function of the porosity. Experimental data from Auracher [36].

4.1. Discretization

The pair $\{T, \varepsilon_v\}$ is solved using the finite volume method. Time derivatives are discretized with a first order implicit Euler scheme. Discretization of face values at previous time instant t^n is performed with Central Difference Schemes (CDS), whereas face values at current time t^{n+1} are dealt with diffusive schemes i.e. first order Upwind Differential Schemes (UDS) due to instabilities that may arise near the wall. In addition, the grid velocity is evaluated at the faces of the swept volume:

$$\vec{v}_b = \frac{{}^{\ell}\vec{r}^{\,n+1}_{f,\text{centroid}} - \vec{r}^{\,n}_{f,\text{centroid}}}{\Delta t} \tag{27}$$

where the face centroid positions $\vec{r}_{f,\text{centroid}}$ are evaluated at the iteration itself and at the former time step, respectively.

4.2. Methodology

The algorithm, which follows a fully implicit time resolution, is presented in Alg. 1, where ℓ refers to the current outer iteration, and m refers to the inner iteration. The calculation of the temperature and porosity distributions follows a Gauss-Seidel method. α_r refers to the underelaxation factors, implemented as dynamic relaxation factors using the Aitken's Δ^2 method (see Section 4.3).

Algorithm 1 Frost growth - moving mesh method

1: Initial conditions ($t = 0$): $\{\bar{T}_{\text{fl}} = T_w \; ; \; y^0_{\text{fs}} \; ; \; \bar{\rho}^0_{\text{fl}}$ (see Table 5)$\}$
2: New time step Δt (evaluation of instant t^{n+1})
3: Extrapolate ${}^{l}\Delta y^{n+1}_{\text{fs}} = 2.5\Delta y^{n}_{\text{fs}} - 2\Delta y^{n-1}_{\text{fs}} + 0.5\Delta y^{n-2}_{\text{fs}}$
4: Move mesh
5: Calculate T from Eq. 12
6: Update physical properties $(Y_v, \rho_{\text{ha}}, \rho_v, \rho_{\text{da}}, c_{p,i}, \rho_{\text{fl}}, D_{\text{eff}}, \lambda_i, \lambda_{\text{fl}}, \mathcal{C}_{1,2,3,4})$
7: Calculate ε_v from Eq. 5
8: **if** $\frac{\|{}^{m}T^{n+1} - {}^{m-1}T^{n+1}\|}{\|{}^{m-1}T^{n+1}\|} > \delta_2$ **and** $\frac{\|{}^{m}\varepsilon^{n+1} - {}^{m-1}\varepsilon^{n+1}\|}{\|{}^{m-1}\varepsilon^{n+1}\|} < \delta_2$ **then**
${}^{m}T^{n+1,\text{NEW}} = f\left({}^{m-1}T^{n+1}, {}^{m}T^{n+1}, \alpha_r\right)$,
${}^{m}\varepsilon^{n+1,\text{NEW}} = f\left({}^{m-1}\varepsilon^{n+1}, {}^{m}\varepsilon^{n+1}, \alpha_r\right)$,
Go to step 5 **endif**
9: ${}^{m}T^{n+1,\text{NEW}} = {}^{m}T^{n+1}$ and ${}^{m}\varepsilon^{n+1,\text{NEW}} = {}^{m}\varepsilon^{n+1}$
10: Update physical properties $(Y_v, \rho_{\text{ha}}, \rho_v, \rho_{\text{da}}, c_{p,i}, \rho_{\text{fl}}, D_{\text{eff}}, \lambda_i, \lambda_{\text{fl}}, \mathcal{C}_{1,2,3,4})$
11: Calculate $\Delta y^{n+1}_{\text{fs}}$ from Eq. 14
12: **if** $\frac{\|{}^{\ell}\Delta y^{n+1}_{\text{fs}} - {}^{\ell-1}\Delta y^{n+1}_{\text{fs}}\|}{\|{}^{\ell}\Delta y^{n+1}_{\text{fs}}\|} > \delta_1$ **then** Go to step 4 **endif**
13: **if** $t_{\text{sim}} < t_{\text{end}}$ **then** Go to step 2
else End of Simulation **endif**

The dynamic movement of the mesh comprehends steps 4, 11 and 12 of the algorithm. The example shown in Fig. 4 shows the moving mesh pattern

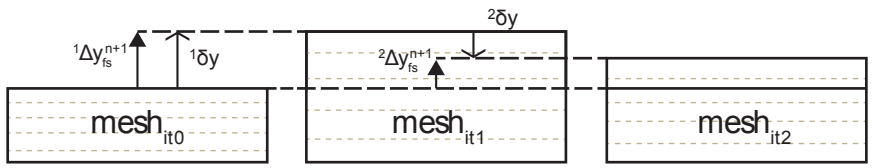

Figure 4: Schematized pattern of a 2-outer-iteration mesh movement.

followed within a time step. Notice that in this particular case, the algorithm goes through step 4 of the algorithm twice before the $\Delta y_{\text{fs}}^{n+1}$ convergence is reached in $\texttt{mesh}_{\text{it2}}$. Equation 28 displays the amount δy that the mesh has to move at a specific outer iteration. While Δy has a physical meaning (recall its definition given in Section 2.3), δy is purely geometrical.

$$^{\ell}\delta y = {}^{\ell}\Delta y_{\text{fs}}^{n+1} - {}^{\ell-1}\Delta y_{\text{fs}}^{n+1} \tag{28}$$

Notice that despite the fact that Δy is positive-definite, δy can take either positive or negative values. No adaptative mesh refinement is used. Thus, the number of control volumes along the simulation remain constant. These are resized after each outer iteration by means of a technique based on a classical elasticity-based mesh update model introduced by Smith and Wright [38] further explained in Appendix.

The $\delta's$ that appear in steps 8 and 12 of the algorithm previously introduced refer to the convergence criteria. The latter are studied along with the time step and the mesh size in order to secure grid independence. The adequate values found are a time step of $10^{-2}s$, and the pair $\{\delta_1 = 10^{-5}, \delta_2 = 10^{-5}\}$ under a single column 30-cell structured mesh.

Different close-to-zero frost layer initial thicknesses are tested. No significant differences are encountered between $y_{\text{fs}}^{0} = 2 \cdot 10^{-5}m$ and $y_{\text{fs}}^{0} = 10^{-5}m$, values also tested by Jones and Parker [39], and later used in [7, 8, 19]. Hence, the present study uses an initial thickness of $10^{-5}m$.

4.3. Relaxation factors

An optimized performance of the model is of key importance as applications with complex geometries and vast domains require large amounts of computational time. This Section tackles the aforementioned by testing two types of relaxation factors for the Gauss-Seidel solver: fixed relaxation factor and Aitken's dynamic relaxation method. Note that these are applied in step 8 of the algorithm previously presented.

Variables are updated at each iteration q as follows:

$$^{q}\mathbf{x} = {}^{q-1}\mathbf{x} + {}^{q-1}\alpha_r \, {}^{q}\mathbf{r} \tag{29}$$

where α_r is the relaxation factor and $\mathbf{r}$ the residual, defined as:

$$^{q}\mathbf{r} = {}^{q}\tilde{\mathbf{x}} - {}^{q-1}\mathbf{x} \tag{30}$$

Parameter	Value-Correlation
μ	{ Auracher [36], Prager [35], Zehnder [33], Bruggeman [35], Le Gall *et al.* [5] with $F = \{1 - 10\}$ with intervals of 0.5}
λ_{fl}	{ Na and Webb [6], Lee *et al.* [32], Negrelli *et al.* [30] }
$\bar{\rho}_{\text{fl}}^{0}$	$\{25, 30, 35\}\ kg/m^3$
P_{fs}	{Saturated, Supersaturated (when applicable)}

Table 5: List of parameters tested in each case.

while $\tilde{\mathbf{x}}$ is the unrelaxed calculated variable.

In fixed relaxation factors, a small enough fixed value is assigned for all iterations to keep a stable solution. On the other hand, dynamic relaxation factors follow Aitken's Δ^2 method as stated in Eq. 31.

$$ {}^{q-1}\alpha_r = -{}^{q-2}\alpha_r \frac{{}^{q-1}\mathbf{r}^T \left({}^{q}\mathbf{r} - {}^{q-1}\mathbf{r}\right)}{\left|{}^{q}\mathbf{r} - {}^{q-1}\mathbf{r}\right|^2} \tag{31} $$

Both fixed and dynamic relaxation factors show a favourable performance and stability. Nevertheless, Aitken's dynamic relaxation method has proved the most efficient based on computational time, taking 50% of the averaged CPU time required by the most adequate fixed relaxation factor.

5. Assessment of the model empirical inputs

The empirical inputs needed by the model, i.e. the diffusion resistance factor, the frost layer conductivity, the initial frost mean density and the pressure condition at the air-frost interface are listed in Table 5. Several empirical correlations and values have been suggested in literature. However, numerical solutions varying the empirical input parameters show significant differences. Such differences urge to conduct parametric studies in order to determine combinations which give best fits against tested experimental data.

The reference experimental cases studied in this paper were chosen with the aim of covering a major region of Hayashi's diagram [2], i.e. covering different types of frost morphologies (see Fig. 5). Taking into account the preference of selecting cases with thickness and average density data over time, the full set of experiments tested by Lee *et al.* [11] were chosen. Moreover, in order to give the study greater generality, the test cases by Sahin [40] were also included. A summary of the experimental conditions is given in Table 6.

Each of these cases is then simulated, by means of 1D numerical tests, with each of the resulting input combinations obtained from Table 5. As an example, an input combination would be Le Gall *et al.* [5] diffusion resistance factor with $F = 2.5$, Na and Webb's [6] frost layer conductivity, an initial frost thickness of $30 kg/m^3$ and a supersaturated condition at the frost-air interface. Note that the heat and mass transfer coefficients are selected based on each specific experiment

Case	W $[kg_v/kg_{\mathrm{da}}]$	T_w [°C]	T_∞ [°C]	v $[m/s]$	Data
`Lee1` [11]	0.00531	-20	10	1.75	$\{y_{\mathrm{fs}}; \bar{\rho}_{\mathrm{fl}}; T_{\mathrm{fs}}\}$
`Lee2` [11]	0.00637	-15	15	2.5	$\{y_{\mathrm{fs}}; \bar{\rho}_{\mathrm{fl}}; T_{\mathrm{fs}}\}$
`Lee3` [11]	0.00323	-15	5	1	$\{y_{\mathrm{fs}}; \bar{\rho}_{\mathrm{fl}}; T_{\mathrm{fs}}\}$
`Sah1` [40]	0.0069	-9.15	12.85	2.11	$\{y_{\mathrm{fs}}\}$
`Sah2` [40]	0.0069	-15.15	12.85	2.11	$\{y_{\mathrm{fs}}\}$
`Sah3` [40]	0.007	-25.15	19.85	2.20	$\{y_{\mathrm{fs}}\}$
`Sah4` [40]	0.0039	-25.15	12.85	2.10	$\{y_{\mathrm{fs}}\}$

Table 6: Chosen experimental conditions and measured data based on Lee *et al.* [11] and Sahin [40] experiments.

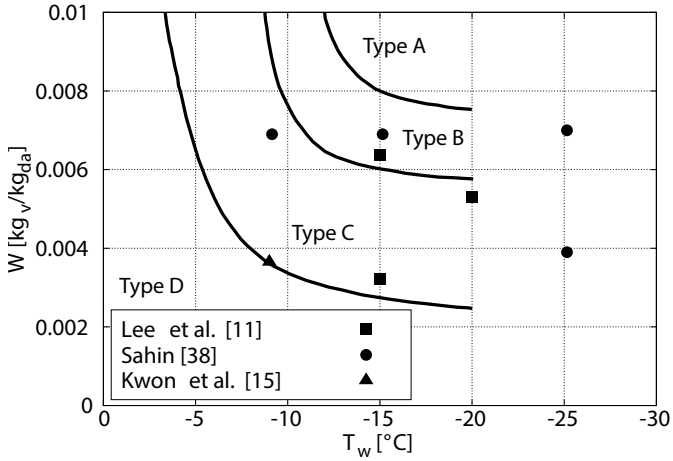

Figure 5: Initial state experimental conditions under Hayashi's $\Delta C - T_w$ diagram[2]. Conditions are given in Tables 6 and 8.

conditions (see Section 5.1). The total amount of input combinations per case is of 414 runs, giving an overall of 2898 runs for the seven cases.

Due to the large number of results, an statistical post-process is made after every simulation in order to find out the best fit of each case. It consists of calculating a modified R-squared value of each output with available experimental data: thickness, mean density and surface temperature over time. The chosen modified R-squared value is given by:

$$R^2_{\mathrm{mod}} \equiv 1 - \frac{\sum_i \left(\mathrm{num}_i - \mathrm{exp}_i\right)^2}{\sum_i \left(\mathrm{exp}_i - \bar{\mathrm{exp}}\right)^2} \tag{32}$$

where $R^2_{\mathrm{mod}} \in (-\infty\,,\,1]$. Recall that a value of 1 correponds to a perfect fit, whereas lowering the R^2_{mod} increases the discrepancies among experimental and numerical data, worsening the output fit. Equation 32 differs from the standard definition in its denominator: instead of dividing by the residuals of the numerical solution, residuals of the experimental data are used in order to share a unique normalization for all the runs tested of a certain case.

Due to the large discrepancies encountered when matching the surface temperature (when available), the criterion followed to find the best fit consists of choosing the combination which maximizes the average of $R_{\mathrm{mod},y_{\mathrm{fs}}}$ and $R_{\mathrm{mod},\bar{\rho}_{\mathrm{fl}}}$. In the cases where no mean density data were reported, the best fit will be given by the combination that maximizes the $R_{\mathrm{mod},y_{\mathrm{fs}}}$.

5.1. Heat and mass transfer coefficients

Lee *et al.* [11] experimental apparatus (cases `Lee1-Lee3`) consisted of a closed wind tunnel, with a test section of 300 mm long, 150 mm wide and 150 mm high. The thickness was measured by a digital micrometer, and the surface temperature with an infrared thermometer. The mean frost density was obtained by weighing the frost mass. The overall uncertainties were of 5.57% in thickness, 6.94% in frost density, and 4.36% in frost surface temperature.

Instead of using an empirical correlation to calculate the Nusselt number, and eventually the heat transfer coefficient, a mass transfer coefficient was first computed from the available experimental data. The latter was extrapolated from every set of thickness, frost mean density and surface temperature given at a certain time. In particular, a mass transfer coefficient can be obtained by means of a mass balance at the interface:

$$\left.\frac{\mathrm{d}\left(y_{\mathrm{fs}}\rho_{\mathrm{fl}}\right)}{\mathrm{d}t}\right|_{t=i} = \left.\left[h_m\left(\rho_{v_\infty} - \rho_{v_{\mathrm{fs}}}\right)\right]\right|_{t=i} \tag{33}$$

where i refers to the instant where the set of data is evaluated, and where $\rho_{v_{\mathrm{fs}}}$ is obtained at the given surface temperature. The heat transfer coefficient is then computed by means of the previously introduced heat and mass transfer analogy (see Eq. 15). The final value is then given by the average of all computed $h_c\,|_{t=i}$.

On the other hand, Sahin [40] experimental set up (cases `Sah1-Sah4`) consisted of an open wind tunnel, with a long entrance rectangular section of 1000 mm long, 254 mm wide and 12.7mm high, followed by a test section of 506 mm

Case	μ	λ_{fl}	$\bar{\rho}_{\text{fl}}^{0}$	P_{fs}	$R^2_{\text{mod},y_{\text{fs}}}$	$R^2_{\text{mod},\bar{\rho}_{\text{fl}}}$
`Lee1`	Le Gall $F = 2$	Negrelli	35	Sat.	0.972	0.960
`Lee2`	Le Gall $F = 3.5$	Na and Webb	35	Sat.	0.951	0.932
`Lee3`	Le Gall $F = 5$	Na and Webb	25	Sat.	0.888	0.701
`Sah1`	Le Gall $F = 6.5$	Na and Webb	35	Sat.	0.962	-
`Sah2`	Le Gall $F = 7$	Na and Webb	35	Sat.	0.995	-
`Sah3`	Le Gall $F = 6.5$	Na and Webb	35	Sat.	0.975	-
`Sah4`	Le Gall $F = 9$	Na and Webb	30	Sat.	0.997	-

Table 7: Best fit cases. Units of $\bar{\rho}_{\text{fl}}^{0}$ are kg/m^3.

long with same aspect ratio. The thickness was measured using two different techniques: using a depth micrometer and the use of a cathetometer. The first being more accurate with an overall uncertainty of ± 0.2 mm.

The averaged Nusselt correlation put forward by Shah (found in [41]) for a thermally developing and hydrodynamically developed flow is hereby used.

$$\text{Nu}_{\text{av}} = \begin{cases} 1.849(L^*)^{-1/3} & \text{for} \quad L^* \leq 0.0005 \\ 1.849(L^*)^{-1/3} + 0.6 & \text{for} \quad 0.0005 < L^* \leq 0.0005 \\ 7.541 + \frac{0.0235}{L^*} & \text{for} \quad L^* > 0.006 \end{cases} \tag{34}$$

where L^* is the dimensionless distance in the flow direction for the thermal entrance region expressed as:

$$L^* = \frac{L}{D_h \text{RePr}} \tag{35}$$

where L is the test section length and D_h the hydraulic diameter.

5.2. Assessment results

The assessment carried out shows that frost layer thickness results can fit properly through numerous combinations. However, fewer combinations capture the rest of the properties with acceptable accuracy (the reader is referred to [42] for a detailed explanation). Testing a model uniquely against frost thickness measurements does not ensure a proper capture of the physical phenomenon. Furthermore, both thickness and frost mean density represent global values of the problem, which are linked together. This is, whenever using parameters that give an increase to the mean frost density, the thickness decreases and viceversa.

The best combination of empirical inputs found for each case, presented in Table 6, is given in Table 7. In addition, a comparison of the numerical solutions and the experimental data is shown in Figs. 6 and 7.

Results ensure that best fits are achieved whenever using diffusion resistance factors above 1. On the other hand, Auracher, Prager, Zehnder and Bruggeman effective diffusivities ($\mu < 1$) show poorer results than Le Gall's correlation,

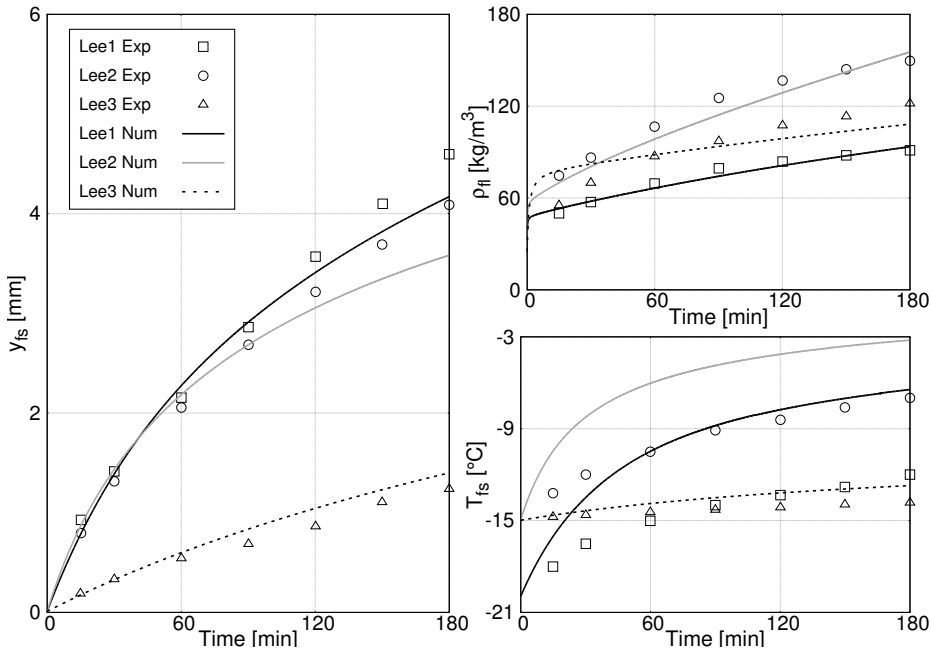

Figure 6: Evolution of the thickness, frost mean density and frost surface temperature of Lee's *et al.* cases.

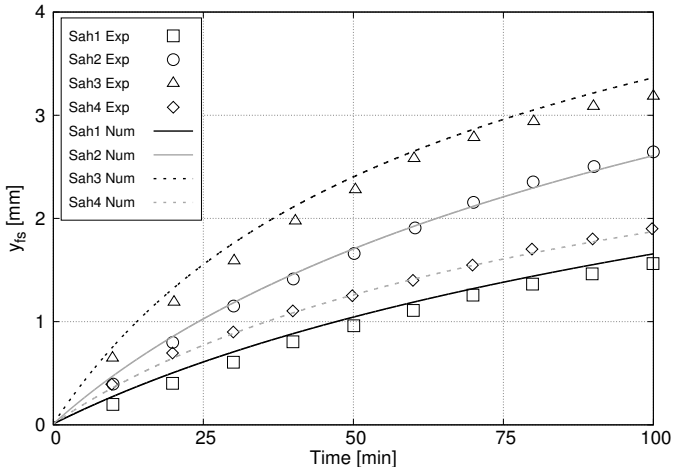

Figure 7: Evolution of the thickness of Sahin's cases.

as these tend to underestimate the total deposited mass. Nevertheless, better agreements are reached when increasing the initial mean frost density, using a supersaturated condition at the air-frost interface (whenever applicable), and also when using Na and Webb's or Negrelli's frost layer conductivity correlations rather than Lee's. This is due to the lower ratio observed between the calculated deposited mass and the experiment deposited mass compared to the one resulting from a $\mu > 1$ effective diffusivity, which is enhanced when imposing the supersaturated condition. This results in the fact that some of the solutions provide good agreement of the frost growth, however lacking a proper capture of the other two variables, which usually follow the tendency line although shifted. Indeed, it is difficult not to underestimate the mean frost density when having a good fit of the frost thickness and viceversa.

5.3. Physical aspects of the diffusion resistance factor

The former numerical assessment shows not only that the chosen effective diffusivity correlation has a great impact in the numerical solution, but also that diffusion resistance factors with values greater than 1.0 are needed to match experimental data. It is found that whenever using correlations which remain within the range $0 \leq \mu \leq 1$, the observed lower ratio between the calculated and the experimental deposited mass unables an accurate capture of the frost growth evolution.

Na and Webb [19] argued the fact that Le Gall and Tao had used values greater than 1.0, stating that such values could not be physically possible. Indeed, no molecule of water vapour can run through a solid wall. Nevertheless, the fact that frost behaves as a packed bed could be a hasty verdict. In his experiments, Yosida [34] found values much greater than 1.0 in snow (which is very similar to frost). He suggested a hand-to-hand delivery of water vapour from side to side of ice crystals. Later on, Tao and Le Gall also found the need of using higher values of the diffusion resistance factors in order to numerically match their own experiments. The latter gave two other physical explanations. First, the displacement of ice crystals towards the cold wall due to the extreme fragility of frost caused by either thermophoresis acting on small ice nuclei, dissociation of dendritic crystals or a modification of the shear stress caused by the air flow along the frost layer. And second, the rate of densification along the frost layer could act as a pumping force, promoting the mass transfer mechanism. Moreover, notice that Le Gall's correlation shown in Fig. 3 follows the trendline of Auracher's at low porosity values, and separates when getting to high porosities. Furthermore, note that the experimental data gathered by Auracher [36] was aquired up to values of $\varepsilon = 0.89$, as shown in Section 3.3. No experimental data has yet been provided in the range of $0.89 < \varepsilon \leq 1$.

Fig. 8 shows the distributions of porosity and temperature at different times of a representative example as a function of a normalized frost thickness. It shows that about 80% of the frost layer has porosity values greater than 0.9, a fact also observed in the frost density distributions computed by Na and Webb presented in [6]. Indeed, this characteristic has been found in all the tested numerical experiments. This is remarkable, as the rate of densification is being

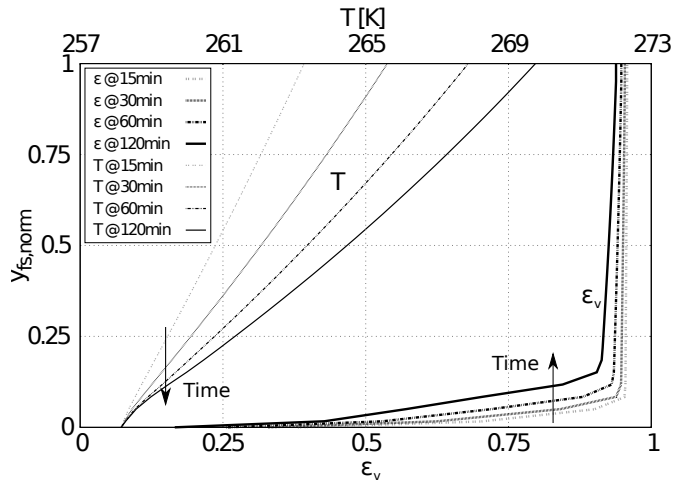

Figure 8: Porosity and temperature distributions in the frost layer over time.

$T_{\text{ha,in}}$ [K]	$v_{\text{ha,in}}$ $[m/s]$	W_{in} $[kg_v/kg_{\text{da}}]$	$T_{w,\text{center}}$ [K]
275.15	1.5	0.00365	264.15

Table 8: Experimental test conditions

held mainly close to the cold wall. It is a fact that not only corroborates the possible mechanisms suggested by Le Gall but also, and most outstanding, the fact that convective effects within the frost layer should be taken into account. In the case convective effects were implemented, a reduction of the maximum values of μ would be expected, as water vapour would penetrate easier into the frost layer. Ongoing work is focused on investigating the validity of such an idea. Furthermore, the lack of experimental data within the frost layer highlights, despite its great difficulties, the actual need to perform experiments aiming to study the internal processes within it.

6. 2D numerical test

The described model, set up through an Arbitrary Lagrangian-Eulerian (ALE) formulation and implemented by means of a finite volume approach, is tested against the experimental case carried out by Kwon *et al.* [17], aiming to complete and verify the conclusions extracted from the previous 1D-studies. The experiment consists of a duct flow with a rectangular cross section of 4mm x 100mm, and a total length of 110 mm. A cooling source is placed at the middle-length cross section of the test chamber, below the aluminum plate that constitutes its bottom side. Fig. 9 shows a detail of the test section. The tested experimental conditions are given in Table 8.

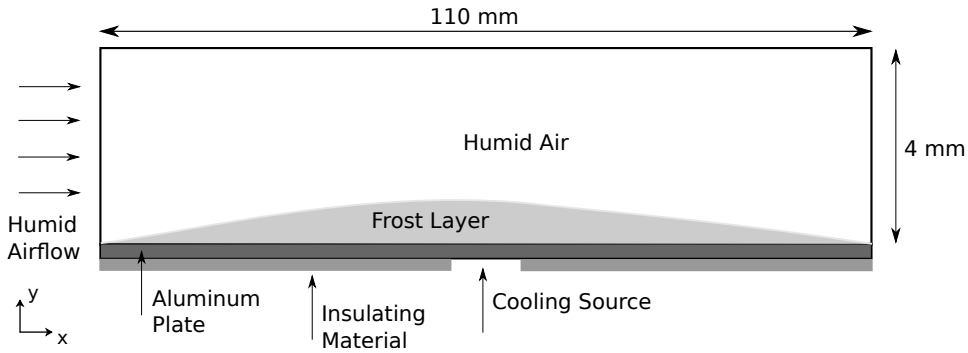

Figure 9: Detail of the test section used by Kwon *et al.* [17].

The total mass of frost was measured every 30 min, until 120 min. Frost thickness was also measured at 7 different locations along the test section. Measures were taken every 30 min, till the end of the experimental test (180 min). The wall temperature, shown in Fig. 10, was also monitored at 17 different positions at 5, 10, 15, 30, 60, 90, 120, 150 and 180 minutes. In order to take into account the temperature variations at the wall boundary, a stepwise Dirichlet type boundary condition consisting of linear interpolations in both streamwise direction and time is implemented.

Following the conclusions extracted from the grid independence study carried out in Section 4.2, the present 2D-study shows the results acquired with a structured mesh of size of 440 x 30 cells, with $\Delta x^0 = 0.25$mm and $\Delta y^0 = 0.33 \cdot 10^{-3}$mm. Note that the growth happens mainly perpendicular to the cold wall. Thus, a small-enough Δx value was chosen such that it would ensure a smooth streamwise transition at the air-frost interface. The model empirical inputs used correspond to `Lee3` case (see Table 7). This combination is chosen due to the fact that among the set of cases studied in Section 5, `Lee3` experimental conditions are the closest to the present study in terms of crystal morphology (see Fig. 5).

On the other hand, as the goal of the present paper is not solving the fluid domain accurately, but to stress out the methodology used to track the interface using a dynamic mesh, a simplified treatment of the flow is applied. Linear functions for the temperature and the water vapour concentration are used along the streamwise direction. The approximate outlet values, $T_{\text{out}} = 274.15K$ and $W_{\text{out}} = 0.00336$, have been taken from a previous numerical test using constant values, and have been qualitatively verified against the available Kwon experimental data.

In addition, local heat and mass transfer coefficients are applied. These are found by means of the local Sherwood number correlation put forward by Lombardi and Sparrow [43], which accounts for the combined entry length problem for parallel plates under a thermally and hydrodynamically developing flow with a wall at a uniform temperature and the other insulated.

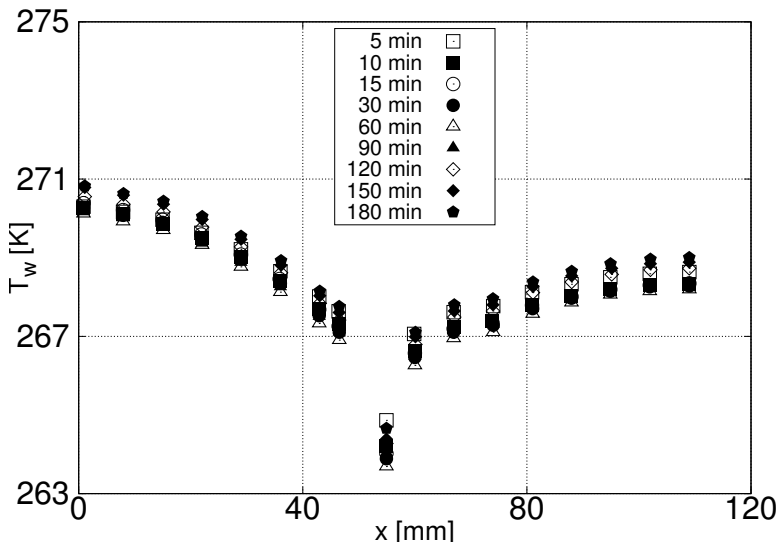

Figure 10: Experimental data aquired by Kwon *et al.* [17], and hereby used as a boundary condition for the cold plate.

$$\mathrm{Sh}_x = 0.332\mathrm{Pr}^{1/3}\left(\frac{\mathrm{Re}}{x/D_h}\right)^{1/2}\left[1+7.3\left(\frac{x/D_h}{\mathrm{Re}}\right)^{1/2}\right]^{1/2} \cdot \left[1+\frac{3.65\left(\frac{x/D_h}{\mathrm{Re}}\right)^{1/2}}{1+7.3\left(\frac{x/D_h}{\mathrm{Re}}\right)^{1/2}}\right] \tag{36}$$

Recall that the Sherwood number is defined as $\mathrm{Sh} = D_h h_m / D_v$.

The steep gradients of the transfer coefficients close to the inlet causes a significant increase of the computational costs. Because of this, a $\mathrm{Sh}_x|_{5\mathrm{mm}}$ is applied when $x \leq 5$ mm.

6.1. Test results

The growth of the frost layer is shown in Fig. 11 through several thickness profiles at different times. The experimental data gathered by Kwon *et al.* [17], and the numerical solutions given by Wu *et al.* [14] using a static grid under a CFD approach, are also depicted.

Results agree well with the experimental data. However, some differences can be observed: an underpredicted growth found in the upstream region, followed by an initial underprediction of the frost growth in the central region. A behaviour also seen close to the outlet.

In the reported experimental facility, the flow is subjected to a sudden stretchment at the inflow of the duct, shown in Fig. 9. The design is such

that higher velocities are found close to the inflow, where a thermal boundary layer is being formed. Thus, increasing the heat and mass transfer coefficients as accounted by Eq. 36. Wu *et al.*'s model does not capture the increase of growth close to the inlet, presumably due to the fact that the simulation domain was extended 5 additional millimeters and, as a consequence, not considering the enhanced gradients of the temperature and the water vapour close to the inlet. On the contrary, despite the fact that the present model indicates a gradual increase of the frost thickness close to the inlet, the underprediction is due to the fact of using constant heat and mass transfer coefficients for the first 5 mm of the duct, previously explained.

Moreover, because the model uses heat and mass transfer coefficients which take into account the hydraulic diameter of the clean duct, the increase of the flow velocity due to the narrowing of the duct caused by the frost growth is not taken into account. Indeed, in the central region, where the velocity is maximized, a larger heat and mass transfer should be expected. Larger heat and mass transfer coefficients would enhance the initial rate of deposition, as seen in the distributions approximately up to 90 min which lay below the experimental values.

Furthermore, the slight overprediction in the downstream region seen in the profiles beginning at 90 min is atributed to the fact of not accounting for a detailed resolution of the water vapour concentration decay along the duct. Recall that the linear profile used would decrease its slope with time, due to the fact of having a reduced deposition of water vapour given by an increase of the surface temperature.

The evolution of the frost weight over time is shown in Fig. 12. Good agreement is found between numerical results and experimental data. Nevertheless, the numerical results show that the deposition tends to slightly decrease with time. This is due to the reduction of the vapour deposition caused by a continuous diminution of the difference between the frost surface and the external flow temperatures, and also between water vapour densities. The aforementioned reducing effect should balance the increase of deposition due to the continuous strangulation of the channel, as the more the frost layer grows, the larger should the heat and mass transfer coefficients be, enhancing the deposition of the water vapour. On the other hand, the high linearity of the numerical solution given by Wu *et al.*'s model implies that the initial rate of deposition of water vapor suffers an increase during the first 30 min of simulation. This is due to the fact that the number of frost cells in contact with humid air along the duct increases gradually, beginning at the central region where the cooling source is located.

In addition, a set of countour plots ranging from 30 to 180 min is shown in Fig. 13. The distributions of the temperature and the porosity show that the regions where the wall temperature is smaller (e.g. the central region), larger growth is reached, and viceversa. However, note that the porosity close to the wall is greater in the central region than in the upstream and downstream areas. This is due to the fact that the rate of phase change in the central region is not sufficient to overcome the increment of the volume due to the frost growth.

Despite the fact that the model is not accounting for a detailed analysis

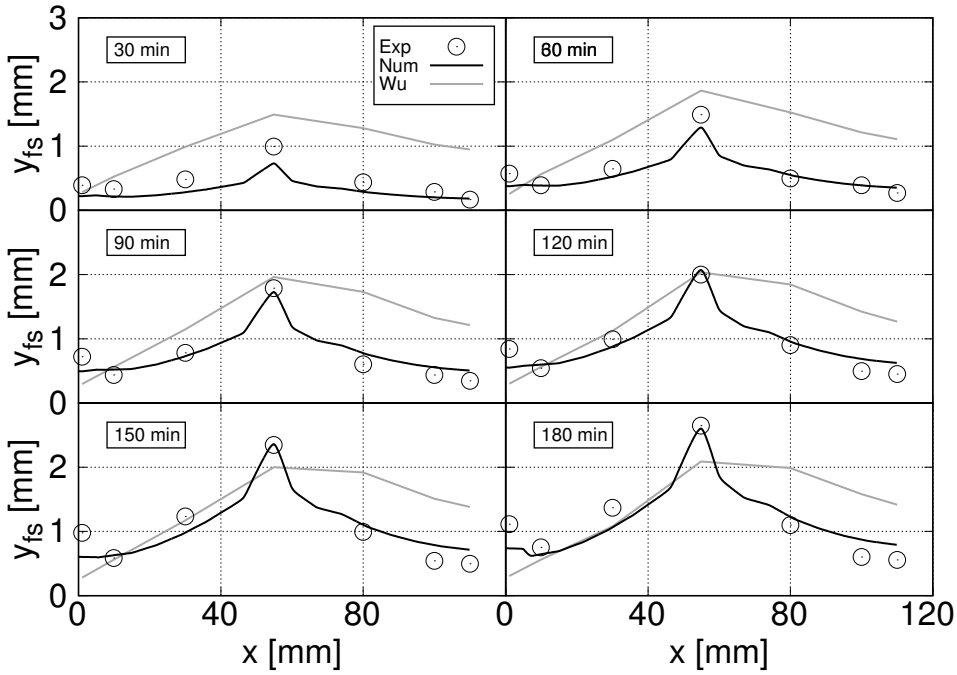

Figure 11: Frost thickness distributions. Comparison of the experimental data acquired by Kwon *et al.* [17] with the present model and Wu's *et al.* [14] model.

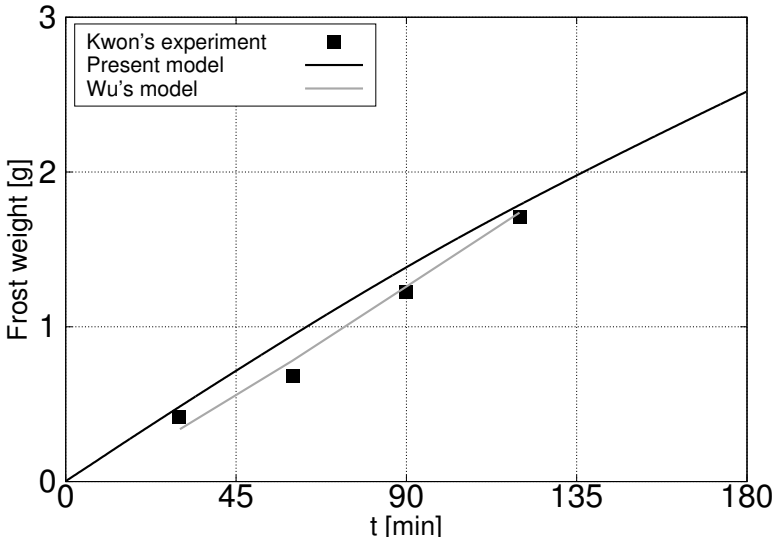

Figure 12: Predicted and measured frost weight.

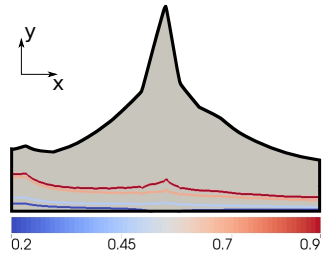

(a) ε_v@30 min, x :1:100, y :1:1

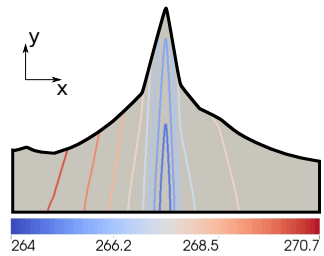

(b) T@30 min, x :1:100, y :1:1

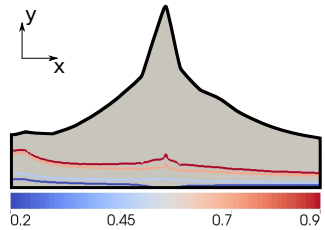

(c) ε_v@60 min, x :1:100, y :1:2

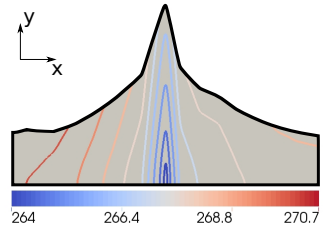

(d) T@60 min, x :1:100, y :1:2

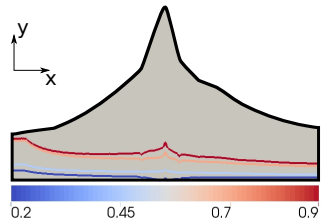

(e) ε_v@120 min, x :1:100, y :1:3.3

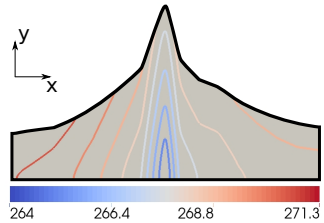

(f) T@120 min, x :1:100, y :1:3.3

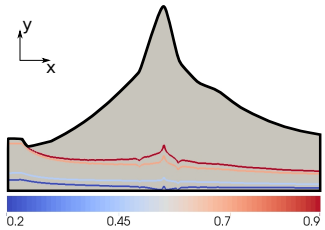

(g) ε_v@180 min, x :1:100, y :1:4

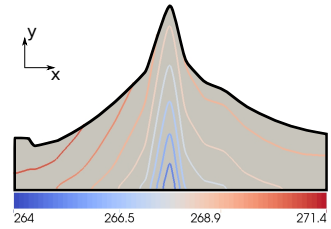

(h) T@180 min, x :1:100, y :1:4

Figure 13: Porosity and temperature contour plots over time. x : and y : refer to the applied image scaling.

of the external humid air flow, but thanks to the interface tracking method implemented by means of a dynamic mesh, the solutions reached show that the presented model is able to produce competitive results, which are in reasonable agreement with the experimental data.

7. Conclusions

A finite volume method capable to solve the frost growth using dynamic meshes has been presented. The model, based on Tao's formulation, takes into account a growing frost domain. The deformation of the mesh is accomplished by means of a moving mesh method that enables the vertices of the mesh to readapt to given imposed displacements at the interface boundary.

Tackling the problem of frost formation is still a challenge. Despite the many empirical correlations proposed in literature, there is still no agreement on which combinations of parameters better capture the formation pattern. A comprehensive numerical assessment of the empirical inputs of the model with seven reference cases has been carried out by means of more than 2800 numerical tests, resulting on combinations which ensure best fits under the considered experimental conditions. Special attention has been given to the arguments upholding the usage of diffusion resistance factors larger than 1.0 when having high porosity values, $\varepsilon_v \geq 0.9$, as they are needed to capute the frost formation. Due to the fact that a significant part of the frost layer has such values, a new insight has been put forward in regards of attributing the water vapour transport inside the frost layer not only to Fickian diffusion, but also to the convective effects involved in it.

Finally, the model has been tested on a bidimensional case with a non-homogeneous temperature at the wall. Notwithstanding the fact that the external flow is not being solved in detail, solutions show reasonable agreement with experimental data, proving the method to be a valid candidate to simulate frost growth.

8. Conflict of interest

None declared.

Acknowledgments

This work has been financially supported by the Research and University Secretary, Department of Business and Knowledge of the Generalitat de Catalunya (2015 DI 0069), and by the Spanish Ministerio de Economía y Competitividad (ENE2015-70672-P). The authors would also like to acknowledge Ignacio González for his contributions to the implementation of the moving mesh method.

Appendix

The implemented moving mesh method that allows deformations of the frost domain is here explained.

The mesh is assumed to be elastic. The linear momentum conservation equation computed at each time step reads as:

$$\cancelto{0}{\frac{\mathrm{D}}{\mathrm{D}t}\int_V \rho \boldsymbol{v} dV} = \oint_S \vec{n} \cdot \boldsymbol{\sigma} dS + \cancelto{0}{\int_V \rho \boldsymbol{f}_b dV}$$

where inertial and body forces are neglected.

Constitutive law

The constitutive equations of a linear, elastic and homogeneous continuum are the Lamé-Hooke equations. In the particular case of small deformations, the stress tensor can be written as follows:

$$\boldsymbol{\sigma} = 2\mu\boldsymbol{\epsilon} + \lambda \mathrm{tr}\left(\boldsymbol{\epsilon}\right) \mathbb{I}$$

where μ and λ are the Lamé coefficients, which can be expressed as a function of Young's modulus and Poisson's ratio. In addition, the infinitessimal strain tensor $\boldsymbol{\epsilon}$ reads as:

$$\boldsymbol{\epsilon} = \frac{1}{2}\left(\nabla\vec{u} + \left(\nabla\vec{u}\right)^T\right)$$

where $\vec{u}$ represents the displacements.

Boundary Conditions

Two main boundary conditions are implemented: Dirichlet (fixed displacement $\vec{u}_B$) and Neumann ($\vec{n} \cdot (\nabla\vec{u}) = 0$) type boundary conditions.

The present study uses Dirichlet type boundary conditions at the wall (with $\vec{u}_B = 0$) and at the frost surface. The side walls use a $\vec{u}_B = 0$ condition in the streamwise direction, and Neumann boundary condition in the other two directions. Periodic walls use a $\vec{u}_B = 0$ in the spanwise direction, and Neumann boundary condition in the other two directions.

Discretization

The momentum equation previously introduced can be written in terms of the displacements using the constitutive law.

$$\oint_S \left(2\mu + \lambda\right) \vec{n} \cdot \nabla\vec{u} dS = \oint_S \vec{n} \cdot \left(\mu \left(\nabla\vec{u}\right)^T + \lambda \mathrm{tr}\left(\nabla\vec{u}\right) \mathbb{I} - \left(\mu + \lambda\right) \nabla\vec{u}\right) dS$$

The left-hand side term, also known as the Laplacian term, is solved implicitly using a central difference scheme with a non-orthogonal correction. On the other hand, the right-hand side term is treated explicitly, and where cell gradients are evaluated by means of a least squares method. The schemes implemented in both sides of the equation ensure second-order accuracy.

Mesh update

Since the model uses a cell-centered finite volume method and the mesh movement is accomplished by updating the vertices, an interpolating function which translates displacements at the cell nodes to displacements at the vertices.

$$\vec{u}_p = \frac{\sum_c \omega_{\mathrm{pc}} \left[\vec{u}_c + (\vec{r}_p - \vec{r}_c) \cdot (\nabla \vec{u})_c\right]}{\sum_c \omega_{\mathrm{pc}}}$$

where p indicates the point where the displacement is interpolated, and c represents the nodes (or cell centers) whose corresponding cell contains point p. The weighting factor ω_{pc} is:

$$\omega_{\mathrm{pc}} = \frac{1}{\|\vec{r}_p - \vec{r}_c\|}$$

Note that $\vec{u}_c$ is equivalent to the δy defined in Eq. 28.

References

[1] Kripa K Varanasi, Tao Deng, J David Smith, Ming Hsu, and Nitin Bhate. Frost formation and ice adhesion on superhydrophobic surfaces. *Applied Physics Letters*, 97(23):234102, 2010.

[2] Y. Hayashi, A Aoki, S Adaohi, and K Hori. Study of frost properties correlating with frost formation types. *Journal of Heat Transfer*, 99(May 1977):239–45, 1977.

[3] P. L. T. Brian, R. C. Reid, and Y. T. Shah. Frost deposition on cold surfaces. *Industrial & Engineering Chemistry Fundamentals*, 9(3):375–80, 1970.

[4] Y.-X. Tao, R.W. Besant, and K.S. Rezkallah. A mathematical model for predicting the densification and growth of frost on a flat plate. *International Journal of Heat and Mass Transfer*, 36(2):353–63, 1993.

[5] R. Le Gall, J.M. Grillot, and C. Jallut. Modelling of frost growth and densification. *International Journal of Heat and Mass Transfer*, 40(13):3177–87, 1997.

[6] Byeongchul Na and Ralph L. Webb. New model for frost growth rate. *International Journal of Heat and Mass Transfer*, 47:925–36, 2004.

[7] Bernard Frankovic Kristian Lenic, Anica Trp. Transient two-dimensional model of frost formation on a fin-and-tube heat exchanger. *International Journal of Heat and Mass Transfer*, 52:22–32, 2009.

[8] JM Armengol, CT Salinas, J Xaman, and KAR Ismail. Modeling of frost formation over parallel cold plates considering a two-dimensional growth rate. *International Journal of Thermal Sciences*, 104:245–256, 2016.

[9] Simon Ellgas and Michael Pfitzner. Modeling frost formation within a commercial 3-d cfd code. *Numerical Heat Transfer, Part A: Applications*, 53(5):485–506, 2007.

[10] Donghee Kim, Chiwon Kim, and Kwan-Soo Lee. Frosting model for predicting macroscopic and local frost behaviors on a cold plate. *International Journal of Heat and Mass Transfer*, 82:135–142, 2015.

[11] Kwan-Soo Lee, Sung Jhee, and Dong-Keun Yang. Prediction of the frost formation on a cold flat surface. *International Journal of Heat and Mass Transfer*, 46(20):3789–96, September 2003.

[12] Chiwon Kim, Jaehwan Lee, and Kwan-Soo Lee. Numerical modeling of frost growth and densification on a cold plate using frost formation resistance. *International Journal of Heat and Mass Transfer*, 115:1055–1063, 2017.

[13] J Cui, WZ Li, Y Liu, and ZY Jiang. A new time- and space-dependent model for predicting frost formation. *Applied Thermal Engineering*, 31:447–457, 2011.

[14] Xiaomin Wu, Qiang Ma, Fuqiang Chu, and Shan Hu. Phase change mass transfer model for frost growth and densification. *International Journal of Heat and Mass Transfer*, 96:11–19, 2016.

[15] Eduard Bartrons, PA Galione, Giorgos Papakokkinos, and Carles D Pérez-Segarra. Fixed-grid numerical modeling of frost formation. In *23rd AIAA Computational Fluid Dynamics Conference*, page 4505, 2017.

[16] Xiaomin Wu, Fuqiang Chu, and Qiang Ma. Frosting model based on phase change driving force. *International Journal of Heat and Mass Transfer*, 110:760–767, 2017.

[17] Jeong-Tae Kwon, Hyo Jae Lim, Young-Chul Kwon, Shigeru Koyama, Dong-Hwi Kim, and Chieko Kondou. An experimental study on frosting of laminar air flow on a cold surface with local cooling. *International Journal of Refrigeration*, 29(5):754–760, 2006.

[18] William Woodside. Calculation of the thermal conductivity of porous media. *Canadian Journal of Physics*, 36(7):815–23, 1958.

[19] Byeongchul Na and Ralph L. Webb. Mass transfer on and within a frost layer. *International Journal of Heat and Mass Transfer*, 47(5):899–911, 2004.

[20] Max Kandula. Frost growth and densification in laminar flow over flat surfaces. *International Journal of Heat and Mass Transfer*, 54:3719–31, 2011.

[21] Amne El Cheikh and Anthony Jacobi. A mathematical model for frost growth and densification on flat surfaces. *International Journal of Heat and Mass Transfer*, 77:604–11, 2014.

[22] S Fukusako. Thermophysical properties of ice, snow, and sea ice. *International Journal of Thermophysics*, 11(2):353–372, 1990.

[23] *ASHRAE Handbook Fundamentals*. American Society of Heating, Refrigerating and Air-conditioning Engineers, Inc., si edition edition, 2009.

[24] T. E. Fessler. *WETAIR - a computer code for calculating thermodynamic and transport properties of air-water mixtures*, volume Tech. Report 1466. NASA, 1979.

[25] Joseph Hilsenrath. *Tables of thermodynamic and transport properties of air, argon, carbon dioxide, carbon monoxide, hydrogen, nitrogen, oxygen and steam*. Pergamon Press, 1960.

[26] Hans R Pruppacher, James D Klett, and Pao K Wang. *Microphysics of clouds and precipitation*. Taylor & Francis, 1998.

[27] Ernst Rudolf Georg Eckert and Robert M Drake Jr. *Analysis of heat and mass transfer*. McGraw-Hill, 1972.

[28] D. R. Lide and H. V. Kehiaian. *CRC Handbook of Thermophysical and Thermochemical Data*. CRC Press, 1994.

[29] Kenneth G Libbrecht. The physics of snow crystals. *Reports on progress in physics*, 68(4):855, 2005.

[30] Silvia Negrelli and Christian JL Hermes. A semi-empirical correlation for the thermal conductivity of frost. *International Journal of Refrigeration*, 58:243–52, 2015.

[31] Florent Breque and Maroun Nemer. Frosting modeling on a cold flat plate: Comparison of the different assumptions and impacts on frost growth predictions. *International Journal of Refrigeration*, 69:340–360, 2016.

[32] K S Lee, T H Lee, and W S Kim. Heat and mass transfer of parallel plate heat exchanger under frosting condition. *Korean Journal of Air-Conditioning and Refrigeration Engineering*, 6(2):155–65, 1994.

[33] C T Sanders. PhD thesis, Technische Hogeschool, Delft (Netherlands), 1974.

[34] Z. Yosida. Physical studies on deposited snow. i: Thermal properties. *Contributions from the Institute of Low Temperature Science*, 7(7):19–74, 1955.

[35] R.E. Cunningham and R.J.J. Williams. *Diffusion in Gases and Porous Media*. New York: Plenum Press, 1980.

[36] H Auracher. Water vapour diffusion and frost formation in capillaries. In *Bulletin of the International Institute of Refrigeration*, pages 477–88, 1972.

[37] Termo fluids s.l., webpage: www.termofluids.com.

[38] Richard W Smith and Jeffrey A Wright. A classical elasticity-based mesh update method for moving and deforming meshes. In *48th AIAA Aerospace Sciences Meeting Including the New Horizons Forum and Aerospace Exposition, Orlando, Florida, Jan. 4-7*, pages 2010–164, 2010.

[39] B.W. Jones and J.D. Parker. Frost formation with varying environmental parameters. *Journal of Heat Transfer*, 97(2):255–259, 1975.

[40] Ahmet Z Şahin. An experimental study on the initiation and growth of frost formation on a horizontal plate. *Experimental Heat Transfer*, 2007.

[41] RK Shah and AL London. *Laminar flow forced convection in ducts: a sourcebook for compact heat transfer exchange analytical data*. Academic Press, 1978.

[42] E Bartrons, CD Perez-Segarra, and C Oliet. Frost formation: Optimizing solutions under a finite volume approach. In *Journal of Physics: Conference Series*, volume 745, page 032062. IOP Publishing, 2016.

[43] G Lombardi and EM Sparrow. Measurements of local transfer coefficients for developing laminar flow in flat rectangular ducts. *International Journal of Heat and Mass Transfer*, 17(10):1135–1140, 1974.